Resetting of the U-Pb and Th-Pb systems in altered bastnäsite: Insight from the behavior of Pb at nanoscale

WEI ZHANG[1], WEI TERRY CHEN[1,2,*], DANIEL HARLOV[3,4,5], AND JIAN-FENG GAO[1,2]

[1]State Key Laboratory of Ore Deposit Geochemistry, Institute of Geochemistry Chinese Academy of Sciences, Guiyang 550081, China
[2]University of Chinese Academy of Sciences, Beijing 100049, China
[3]Deutsches GeoForschungsZentrum GFZ, Telegrafenberg, D-14473 Potsdam, Germany
[4]Faculty of Earth Resources, China University of Geosciences, Wuhan 430074, China
[5]Department of Geology, University of Johannesburg, P.O. Box 524, Auckland Park, 2006, South Africa

ABSTRACT

Bastnäsite contains considerable amounts of U and Th and has been widely used for U-Th-Pb dating. Hydrothermal alteration of bastnäsite is common in nature but its effects on U-Th-Pb dating are not currently well constrained. Hence the significance of U-Th-Pb ages obtained from altered bastnäsite cannot be evaluated. Here, we present a detailed geochronologic as well as micro- and nano-scale mineralogical study of altered bastnäsite in a Mo-REE deposit, Central China. The original bastnäsite grains were confirmed to have crystalized at 208 Ma but were variably overprinted by a hydrothermal event at 150 Ma. They commonly exhibit typical replacement textures that appear to have formed from a coupled dissolution-reprecipitation process, i.e., a primary unaltered domain surrounded by a porous altered domain. Micro- and nano-scale mineralogical observations strongly suggest that during the coupled dissolution-reprecipitation process, non-radiogenic (common) Pb was incorporated into the altered domains in the form of nanoscale galena inclusions. Such incorporation (even minor) has significantly affected the $^{206}Pb/^{238}U$ and $^{207}Pb/^{206}Pb$ ratios due to the low contents of U and its daughter isotopes in bastnäsite, resulting in highly variable, discordant U-Pb dates for the altered domains. In contrast, incorporation of the non-radiogenic Pb has very limited effects (<5%) on the Th-Pb system due to the remarkably high contents of Th and radiogenic ^{208}Pb in bastnäsite. Instead, the scattered $^{208}Pb/^{232}Th$ ages (208 to 150 Ma) of the altered domains were essentially affected by incomplete replacement, and thus can be used to approximate the lower age limit of the primary hydrothermal activity or the upper age limit of the secondary hydrothermal activity. The results from this study highlight that because of the different orders of magnitude between the U and Th contents in bastnäsite, the mobilization of radiogenic and non-radiogenic Pb during alteration may have significantly different impacts on the U-Pb and Th-Pb systems. Therefore, the two systems should be treated separately during the dating of bastnäsite resulting from secondary hydrothermal events.

Keywords: Bastnäsite, dissolution-reprecipitation, reset, U-Th-Pb ages, Huangshuian Mo-REE deposit

INTRODUCTION

Bastnäsite $(Ce,La,Nd,Y)(CO_3)F$ is the most important ore mineral in REE deposits, providing ~51% of rare-earth oxide reserves worldwide (Jordens et al. 2013; Weng et al. 2015). It contains considerable amounts of U and Th with negligible initial uptake of Pb, and is suitable for U-Th-Pb dating. Since the pioneering work of Sal'nikova et al. (2010), U-Th-Pb dating of bastnäsite has been widely applied to constrain the age of REE mineralization (e.g., Yang et al. 2014; Smith et al. 2015; Ling et al. 2016; Zhang et al. 2019).

Secondary hydrothermal activity can significantly upgrade the ores of REE deposits by remobilization and precipitation of REEs, such as that in the Bayan Obo Fe-REE-Nb deposit (Song et al. 2018; Li et al. 2021) and Miaoya REE-Nb deposits (Ying et al. 2020; Ma et al. 2021). Therefore, precise determination of the timing of secondary hydrothermal activities in REE deposits is critical for understanding the mineralization. Bastnäsite has been confirmed to be reactive in the presence of hydrothermal fluid (Li et al. 2021). It may contain textural, chemical and isotopic zoning, which represent multiple hydrothermal events. When different domains in the minerals are dated, the history of a rock sample may be reconstructed. Assessing the reliability or geological significance of U-Th-Pb ages from these altered domains depends largely on the behavior of Pb during replacement (Williams et al. 2011; Seydoux-Guillaume et al. 2012; Harlov et al. 2011; Didier et al. 2013; Grand'Homme et al. 2016). Only if the radiogenic Pb in the metasomatized area was totally removed, would the age be fully reset and record the timing of alteration. However, the behavior of Pb during alteration of bastnäsite and how it affects U-Th-Pb ages has been poorly addressed, and thus the geological significance of U-Th-Pb dates obtained from

465

altered domains cannot be evaluated.

In this contribution, we provide evidence for the modification of U-Th-Pb systems in bastnäsite during the hydrothermal alteration of the Huangshuian Mo-REE deposit from southern margin of the North China Craton, Central China (Fig. 1). Precise molybdenite Re-Os dating has revealed two episodes of hydrothermal activity in the deposit (Li 2014). Bastnäsite originally crystallized during the early episode but was variably altered by the fluids during the later episode (Zhang et al. 2019). The behavior of Pb during the replacement is investigated on both the micro- and nanoscale. The results from this study explain the origins of varied U-Th-Pb dates in the altered bastnäsite, which have broad implications for the dating of secondary hydrothermal activities in other REE deposits.

Regional geology

The southern margin of the North China Craton is bounded by the San-Bao fault to the north and the Luanchuan fault to the south (Fig. 1a). It consists of Archean to Paleoproterozoic high-grade metamorphic basement variably overlain by unmetamorphosed marine sedimentary rocks of Mesoproterozoic to late Paleozoic age (Fig. 1a). The basement is the widespread Taihua Group with age of 2.84 to 1.97 Ga (Kröner et al. 1988; Zhang et al. 2001). It is comprised dominantly of amphibolite, felsic gneiss, migmatite, and metamorphosed supracrustal rocks. The Taihua Group is unconformably overlain by the Paleoproterozoic Xiong'er Group, which is a well preserved, unmetamorphosed volcanic sequence composed of a thick sequence of volcanic rocks ranging in composition from basalt to rhyolite with minor intercalations of clastic rocks (Zhao et al. 2002; Peng et al. 2008). Zircon U-Pb dating reveals that volcanic rocks of the Xiong'er

Group were erupted from 1.78 to 1.45 Ga (He et al. 2009; Zhao et al. 2009). The Xiong'er Group is locally unconformably overlain by Mesoproterozoic strata which consist of marine carbonates and clastic rocks. Intrusions are widespread in the region and were generated by the continental convergence between the North China Craton and the South China Craton during the Mesozoic (Wu and Zheng 2013; Dong and Santosh 2016). These Mesozoic intrusions are dominated by granitic plutons and porphyry dikes with minor alkaline rocks and carbonatites, and are responsible for the widespread Mo and Au mineralization in the region (Mao et al. 2011; Deng et al. 2014; Li and Pirajno 2017).

Geology of the Mo-REE deposit

The Huangshuian Mo-REE deposit is located at the center of the Xiong'ershan region in the southern margin of the North China Craton (Fig. 1a). It is unique with respect to the coexistence of both Mo and REE mineralization (Kynicky et al. 2012; Song et al. 2016; Zhang et al. 2019, 2021). Outcrop in the deposit is the Shibangou Formation of the Taihua Group, which consists of biotite plagiogneiss, amphibole plagiogneiss, and migmatite gneiss (Fig. 1b). These metamorphic rocks were intruded by quartz porphyry, granitic porphyry, diorite, and carbonatites (Fig. 1b). The Huangshuian Mo-REE deposit is spatially associated with carbonatites which occur as plugs and dikes in the metamorphic rocks. These carbonatites are composed dominantly of calcite (70%), quartz (15%), and K-feldspar (5%) with subordinate barite, fluorite, biotite, apatite, pyrite, and magnetite. The ore bodies are lenticular in shape (50–1000 m long) and strike northwest with steep dips of ~80°N (Fig. 1b). The Mo-REE mineralization in the deposit is characterized by abundant hydrothermal veins crosscutting the carbonatites and/or the metamorphic rocks. Based on field observations, two major types of veins are identified, including early quartz-calcite-fluorite and late quartz-pyrite veins (Fig. 2). Molybdenite Re-Os dating has revealed that the two types of veins were formed at 208 and 150 Ma (Li 2014).

The early quartz-calcite-fluorite veins are ubiquitous in the carbonatites (Fig. 2a) and are the major hosts of Mo-REE mineralization. They are proposed to have formed from the hydrothermal fluids derived from carbonatitic magmas (Zhang et al. 2019, 2021). These veins are present as stockworks with thicknesses ranging from 1 to 10 cm. They are composed of quartz, calcite, barite, and fluorite with variable amounts of fluorapatite, pyrite, magnetite, molybdenite, bastnäsite, parisite, and monazite (Fig. 2c). Molybdenite is mainly present as thin, platy, euhedral to subhedral crystals and/or disseminated grains (Fig. 2c). Bastnäsite is the dominant REE mineral and occurs as euhedral to anhedral grains with diameters varying from 10 to 200 μm; it is closely associated with molybdenite in the veins. The bastnäsite grains are overprinted by the quartz-pyrite veins and commonly exhibit complex internal textures that consist of unaltered and altered domains under backscatter electron images (Fig. 3).

The late quartz-pyrite veins, locally crosscutting the early quartz-calcite-fluorite veins (Fig. 2b), are relatively minor and occur mainly in the northwest section of the Huangshuian mine (Li 2014). These veins are synchronous with the widespread porphyry-associated Mo mineralization in the region (Mao et al. 2008, 2011). They are generally straight with a thickness >3 cm
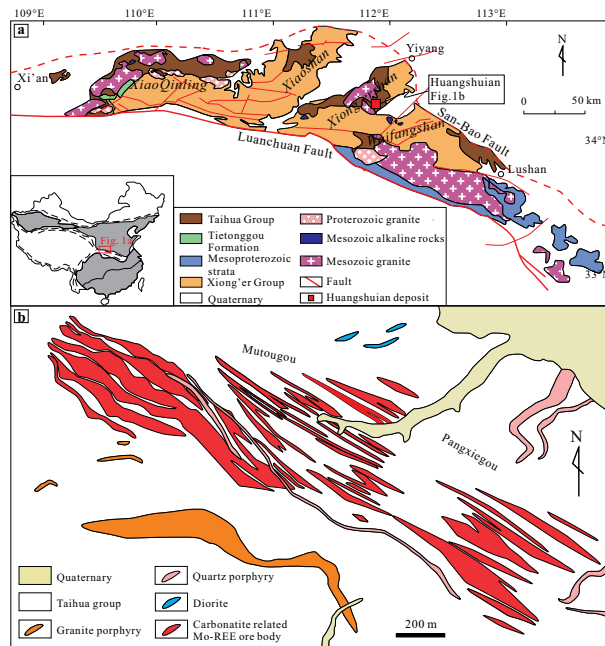

FIGURE 1. (a) Geological sketch of the southern margin of the North China Craton and the location of the Huangshuian Mo-REE deposit. (b) Simplified geological map of the Huangshuian Mo-REE deposit.
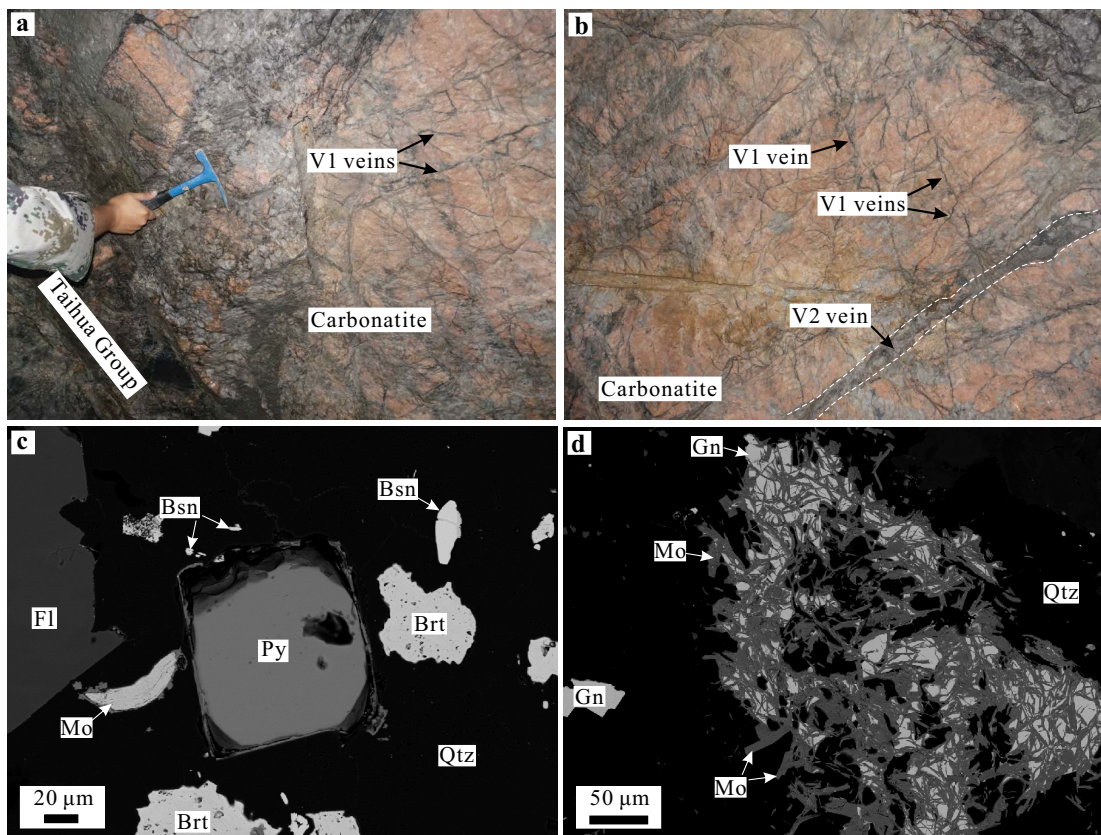
FIGURE 2. (**a**) Early quartz-calcite-fluorite veins (V1 veins) occur as stockworks crosscutting the carbonatites. (**b**) Late quartz-pyrite veins (V2 vein) crosscut early quartz-calcite-fluorite veins. (**c**) The intergrowth of quartz, fluorite, barite, pyrite, molybdenite, and bastnäsite in the early quartz-calcite-fluorite veins. (**d**) The intergrowth of galena and molybdenite in the late quartz-pyrite veins. Abbreviations: Bsn = bastnäsite; Qtz = quartz; Py = pyrite; Mo = molybdenite; Fl = fluorite; Brt = barite; Gn = galena.

and are composed dominantly of quartz (90%) with minor and variable amounts of pyrite, galena, sphalerite, and molybdenite (Fig. 2d). Galena is ubiquitous in the veins and present as cubic grains, while molybdenite is mainly present as euhedral platelets (Fig. 2d). The late quartz-pyrite veins are generally free of bastnäsite.

ANALYTICAL PROCEDURES

Backscatter electron (BSE) imaging

Backscatter electron (BSE) imaging was conducted on polished thin sections using a JSM-7800F thermal field scanning electron microscope (SEM) equipped with TEAM Apollo XL energy-dispersive X-ray spectrometer and a Mono CL4 Cathodoluminescence spectroscope at the State Key Laboratory of Ore Deposit Geochemistry, Institute of Geochemistry, Chinese Academy of Sciences, Guiyang, China. Polished thin sections were carbon coated, and the instrument operated at an acceleration voltage of 15 kV and a probe current of ~10 nA.

Electron probe microanalysis (EPMA)

Major element concentrations of the bastnäsite were determined using a JEOL JXA-8530F field emission electron probe microanalyzer (EPMA) at the State Key Laboratory of Ore Deposit Geochemistry. The analyses were performed with a beam spot diameter of 5 µm, a beam current of 20 nA, and an acceleration voltage of 15 kV. The analyzing crystals were PETH (K, Cl, Th, Ca), LiFH (Pr, Sm), LDE1 (F), TAP (Na, Y), and LIFL (La, Ce, Nd, Gd, Dy, Eu, and Tb). The $K\alpha$ line was chosen for the measurement of K, Cl, Ca, Fe, Na, F; $M\alpha$ line for Th; $L\alpha$ line for Y, La, Ce; and $L\beta$ line for Pr and Sm, Nd, Gd, Dy, Eu, and Tb. The counting times for the

peaks were 10 s for K, Cl, Fe, Na, F, and 30 s for the other elements. Background intensity was measured on both sides of the peak with half the counting time for the peak. Standards used for analyses include orthoclase for K_2O and Al_2O_3, plagioclase for Na_2O, tugtupite for Cl, topaz for F, and monazite for ThO_2, CaO, Pr_2O_3, Sm_2O_3, Y_2O_3, La_2O_3, Ce_2O_3, Nd_2O_3, Gd_2O_3, Dy_2O_3, Eu_2O_3, Tb_2O_3, Pyrope for FeO. Under these conditions, the detection limits were approximately 50 to 100 ppm for K, Cl, and Ca; 100 to 300 ppm for Na, Th, and Fe; 300–500 ppm for REEs (including Y); and 500 to 700 ppm for F.

In situ laser ablation inductively coupled plasma mass spectrometer (LA-ICP-MS) trace elemental analysis

In situ trace element analyses of bastnäsite were conducted by LA-ICP-MS at the Wuhan Sample Solution Analytical Technology Co., Ltd., Wuhan, China. Operating conditions for the laser ablation system and the ICP-MS instrument and data reduction have been described in detail in Zong et al. (2017) and thus are briefly summarized here. Laser sampling was performed using a GeolasPro laser ablation system that consists of a COMPexPro 102 ArF excimer laser (wavelength of 193 nm and maximum energy of 200 mJ) and a MicroLas optical system. An Agilent 7700e ICP-MS instrument was used to acquire ion-signal intensities. Helium was applied as a carrier gas. Argon was used as the make-up gas and mixed with the carrier gas via a T-connector before entering the ICP. A "wire" signal smoothing device is included in this laser ablation system (Hu et al. 2015). The spot size and frequency of the laser were set to 32 µm and 10 Hz, respectively. Trace element compositions of minerals were calibrated against various reference materials (BHVO-2G, BCR-2G, and BIR-1G) without using an internal standard (Liu et al. 2008). MACS-3 was used as a second standard to ensure accurate results. Each analysis incorporated a background acquisition of approximately 20–30 s followed by 50 s of data acquisition from the sample. An Excel-based software ICPMSDataCal was used to perform offline selection and integration of background

FIGURE 3. Backscattered electron (BSE) images of altered bastnäsite in the Huangshuian deposit. (**a**) Bright, homogeneous unaltered domains surrounded by dark, inhomogeneous altered domains. Also shown is the location of the FIB cut foil (white rectangle). Inclusions with the brightest BSE intensity in the altered domains include thorite and galena. (**b**) Abundant galena inclusions with variable diameters up to 5 μm in the altered domains. (**c**) Bastnäsite preserve its original morphology after alteration. Also shown is the location of analyzed spots in both the altered and unaltered domains. (**d**) Small patches of primary bastnäsite distributed in the matrix of the secondary bastnäsite. Abbreviations: Th = thorite; Qtz = quartz; Ga = galena.
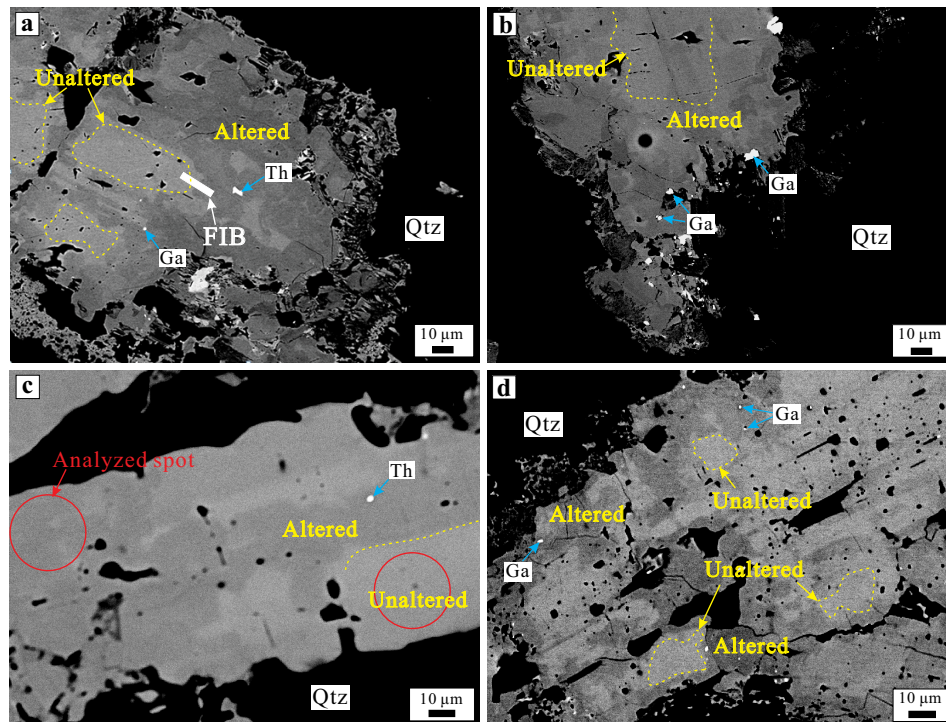
and analyzed signals, time-drift correction, and quantitative calibration for trace element analysis (Liu et al. 2008).

LA-ICP-MS U-Th-Pb isotopic analyses

The U-Th-Pb isotopic analyses of bastnäsite in polished thin sections were carried out using an inductively coupled plasma mass spectrometer (ICP-MS) (Agilent 7700×) with a laser ablation (LA) system (ASI RESOnetics S-155, 193 nm wavelength) (LA-ICP-MS) at the Nanjing FocuMS Technology Co. Ltd, Nanjing, China. Detailed analytical procedures and instrumental operating conditions are available in Yang et al. (2014, 2019) and Ling et al. (2016) and are briefly summarized here. Analyses were performed with a beam diameter of 24 μm and a repetition rate of 6 Hz. At the start of each analytical session, the torch position and lens tuning were adjusted to maximize the sensitivity for the appropriate masses (Pb isotopes, Th and U) and stability. To minimize the production of molecular compounds, ThO^+/Th^+ was monitored to avoid exceeding 0.3%. Each spot analysis consisted of an ~20 s of background acquisition and 60 s of sample data acquisition. Bastnäsite K-9 (118 ± 1 Ma, MSWD = 0.05, probability = 0.82), which is currently the only standard for bastnäsite U-Th-Pb dating (Sal'nikova et al. 2010), was used to correct U-Th-Pb fractionation and instrumental mass discrimination of the bastnäsite. Two analyses of the standard were measured after every five unknown bastnäsite spots. Signals of ^{204}Pb, ^{206}Pb, ^{207}Pb, ^{208}Pb, ^{232}Th, and ^{238}U were acquired for U-Th-Pb dating, whereas the ^{235}U signal was calculated from ^{238}U on the basis of a $^{238}U/^{235}U$ ratio of 137.88. Offline data selection and integration were performed by using ICPMSDataCal software (Liu et al. 2010), and age calculations were performed using ISOPLOT (Ludwig 2003). Uncertainties associated with age determinations are 2σ at 95% confidence level.

Focused ion beam (FIB) and transmission electron microscopy (TEM) analyses

The FIB preparation was conducted on FEI Scios Dual beam at the Center for Lunar and Planetary Sciences, Institute of Geochemistry, Chinese Academy of Sciences, Guiyang, China. The FEI Scios Dual Beam combines a traditional field emission electron column with a FIB column and is equipped with energy-dispersive X-ray spectroscopy (EDS) and electron backscattered diffraction (EBSD) detectors. Fabrication and extraction of the TEM foil follows the procedure outlined in Wirth (2004). The altered bastnäsite grains were first examined with BSE imaging to select a representative cross-section perpendicular to the reaction front where the TEM foil was cut. A 2 μm thick Pt layer was deposited onto the selected foil to protect it from sputtering by the Ga-ion beam. Two larger trenches were milled in front and behind

the foil with a high Ga-ion current (15 nA). Milling was continued with a reduced Ga-ion beam size (reduced beam current, 1 nA) until the foil thickness was ~500 nm. At that stage, the specimen was tilted 45° with respect to the Ga-ion beam, and the foil cut free at its base and on both sides, leaving only a narrow (ca. 1 μm) strip of material to fix the foil in its position. Subsequently, stabilization strips on both sides are cut, and the foil is placed onto the membrane of a TEM copper grid. Finally, the foil was finely milled and polished (48 pA) until the thickness was <100 nm.

The TEM analyses were performed using a FEI Talos F200S, operated at an accelerating voltage of 200 kV at the Analysis and Test Center, Guangdong University of Technology, Guangdong, China. The high-resolution TEM (HRTEM) study was performed using a Gatan Quantum electron energy loss spectrometry (EELS) accessory. Compositional analysis of nano-sized minerals was conducted using an energy-dispersive X-ray spectrometer (EDXS). Analytical conditions include a 1 nA beam current and a ~5 nm beam size in the STEM mode. Accumulation time of X-ray signals was 5 s per analysis.

RESULTS

Bastnäsite textures

The SEM investigations reveal that the unaltered and altered domains of bastnäsite exhibit obviously different internal textures (Fig. 3). The unaltered domain is BSE-bright, homogeneous, and free of mineral inclusions. It generally occurs at the center of the crystals (Figs. 3a–3b). In some severely altered grains, it is present as small patches surrounded by the altered domains (Fig. 3d).

The altered domain is relatively BSE-dark and commonly occurs at the margins of the crystals or along fractures (Fig. 3). Its brightness is highly variable in the high-contrast BSE images and generally negatively correlated to the intensity of the alteration. The altered domain contains abundant pores and voids that are filled with quartz, calcite, and fluorite (Figs. 3a–3c). Mineral inclusions in the altered domains include thorite and galena, both of which have a high brightness in the BSE images (Fig. 3). Thorite occurs as sub-round grains with diameters generally smaller than 2 μm (Fig. 3c), whereas galena is present as euhedral to subhedral grains with diameters of up to 5 μm (Figs. 3a–3b).

Bastnäsite compositions

The EPMA major and LA-ICP-MS trace element compositions of the unaltered and altered domains of bastnäsite are provided in Online Materials[1] Tables OM1 and OM2, respectively. EPMA mapping of different elements is presented in Figure 4, which shows that the unaltered and altered domains have different compositions.

The unaltered domains have broadly homogeneous compositions. The total REE_2O_3 content varies from 69.7 to 72.2 wt%. The REEs are dominated by light rare earth elements (LREE), of which La_2O_3, Ce_2O_3, Pr_2O_3, and Nd_2O_3 have contents varying from 25.6 to 28.0 wt%, 33.4 to 35.2 wt%, 2.1 to 2.5 wt%, and 6.4 to 7.2 wt%, respectively. Middle rare earth elements (MREE) and heavy rare earth elements (HREE) have concentrations generally <0.5 wt% (Online Materials[1] Table OM1). The La/Ce (apfu) ratios are relatively constant (0.73 to 0.84) (Online Materials[1] Table OM1). The concentrations of Th and U in the unaltered domains vary from 3594 to 5046 ppm (average of 4302 ppm) and 37 to 71 ppm (average of 49 ppm), respectively (Online Materials[1] Table OM2).

The compositions of the altered domains are highly variable (Fig. 5). The total REE_2O_3 content (70.1 to 72.4 wt%) is similar to those of the unaltered domains. However, compared to the unaltered domains, the altered domains have much higher contents of La_2O_3 (26.6 to 38.7 wt%) and lower contents of Ce_2O_3 (27.9 to 34.6 wt%), Pr_2O_3 (1.39 to 2.44 wt%), Nd_2O_3 (3.34 to 7.11 wt%), Sm_2O_3 (<0.385 wt%), Gd_2O_3 (0.019 to 0.315 wt%), and Y_2O_3 (<0.31 wt%). The La/Ce (apfu) ratios are highly variable from 0.78 to 1.40 (Online Materials[1] Table OM1). The concentrations of Th and U are both lower than those of the unaltered domains, varying from 2482 to 3312 ppm (average at 2932 ppm) and 19 to 33 ppm (average at 23 ppm), respectively (Fig. 5d).

U-Th-Pb geochronology of bastnäsite

The U-Th-Pb geochronologic results of bastnäsite are provided in Online Materials[1] Table OM3 and illustrated in Figures 6 and 7. For the unaltered domains, 27 analyses of uncorrected data give a lower intercept age of 210.2 ± 4.5 Ma (MSWD = 2.3) on the Tera-Wasserburg plot (Fig. 6a). After correction for common Pb by the 207-based method (assuming the $^{207}Pb/^{206}Pb$ of Pb_0 is the y-intercept in the Tera-Wasserburg plot; Schoene 2014), a weighted average $^{206}Pb/^{238}U$ age of 209.4 ± 3.6 Ma (MSWD = 2.7; n = 27) is obtained (Fig. 6b). The weighted average $^{208}Pb/^{232}Th$ age is calculated to be 203.8 ± 1.5 Ma (MSWD = 3.8; n = 27) (Fig. 7a). These ages are compatible with the molybdenite Re-Os age (~208 Ma) of the early quartz-calcite-fluorite veins (Cao et al. 2014; Li 2014).

Analyzed spots in the altered domains were carefully selected to avoid pores and solid inclusions. Here the altered domains show greater scatter in the U-Th-Pb dates. Compared to the unaltered domains, the altered domains have significantly higher $^{206}Pb/^{238}U$ and $^{207}Pb/^{206}Pb$ ratios, corresponding to significantly
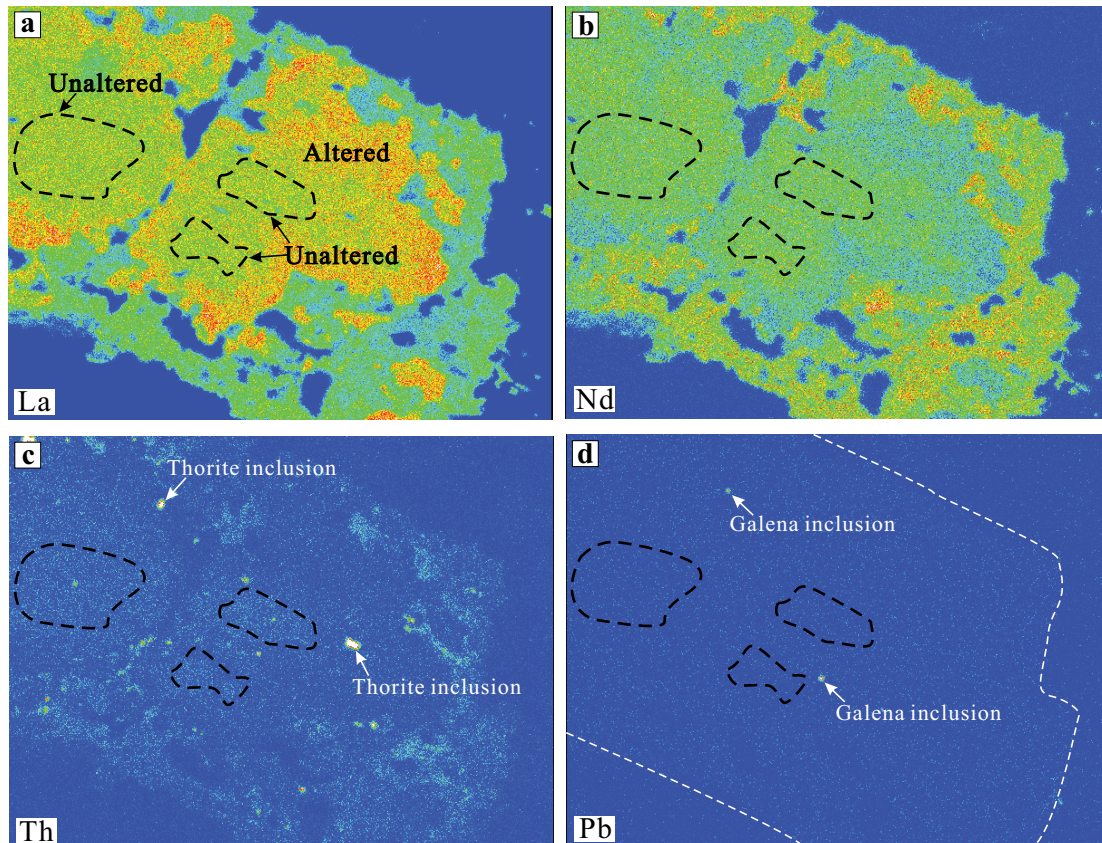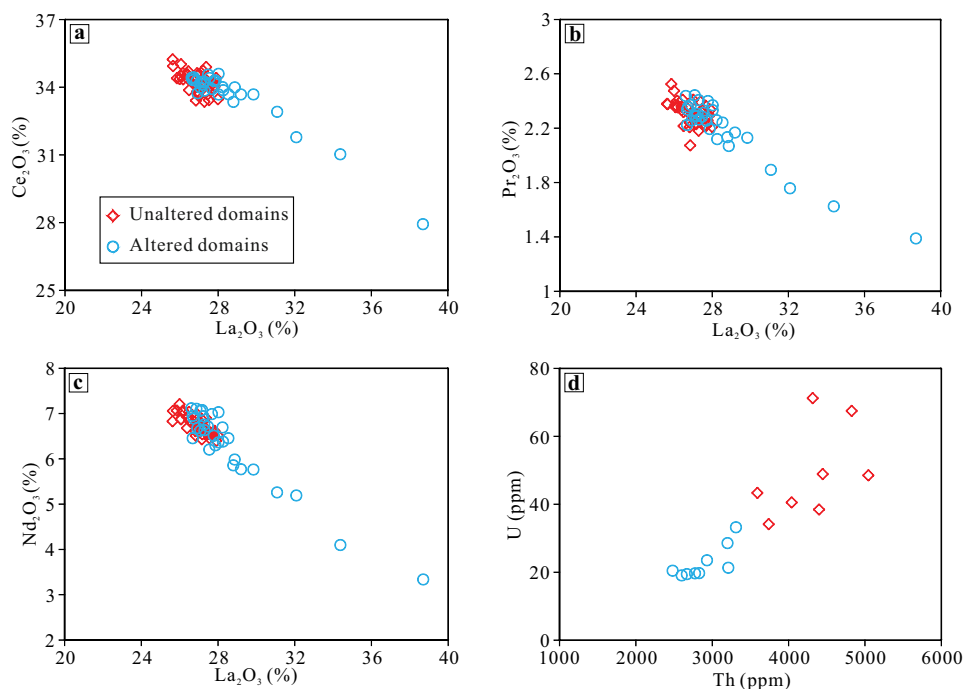

FIGURE 4. EPMA element mapping of (**a**) La, (**b**) Nd, (**c**) Th, and (**d**) Pb in the altered bastnäsite in Figure 3a. Note that the bright spots in **c** and **d** are thorite and galena inclusions, respectively.

FIGURE 5. Plots of (**a**) La_2O_3 vs. Ce_2O_3, (**b**) La_2O_3 vs. Pr_2O_3, (**c**) La_2O_3 vs. Nd_2O_3, and (**d**) Th vs. U for different domains in the bastnäsite.

variable $^{206}Pb/^{238}U$ and $^{207}Pb/^{206}Pb$ ages (Online Materials[1] Table OM3). On the Tera-Wasserburg plot, they deviate from the concordia curve and are irregularly distributed (Fig. 6c). On the other hand, the $^{208}Pb/^{232}Th$ ages are strictly scattered from 208 to 150 Ma, which fall in the range between the molybdenite Re-Os ages of the early quartz-calcite-fluorite veins and the late quartz-pyrite veins (Fig. 7b).

Nano-structural study

Focused Ion Beam (FIB) foils were cut at the interface between the unaltered and altered domains for examining of the nanoscale textures (Fig. 3a). TEM investigation reveals that the unaltered and altered domains can be distinguished in terms of nanoscale structures (Fig. 8). The unaltered domains are totally crystalline without any porosity or inclusions (Fig. 8a). They have continuous lattice fringes in high-resolution TEM images (Fig. 9). In contrast, the altered domains are characterized by the occurrence of abundant nanoscale channels and voids (Figs. 8b–8c). Nano-channels, which have widths of about 20 nm, are generally straight and parallel to each other (Fig. 8b). Nano-voids are typically sub-rounded in shapes, with diameters ranging from 5 to 50 nm (Fig. 8c). Locally, the nano-voids are present at the transections of several nano-channels (Fig. 8c). Minor 20 nm size inclusions of galena are also seen in the altered domains (Fig. 8d). High-resolution TEM images reveal that the altered domains remain crystalline, but their lattice fringes are frequently distorted with a random orientation (Fig. 9).

DISCUSSION

Incorporation of non-radiogenic common Pb during the coupled dissolution-reprecipitation process

Preservation of the original morphology (pseudomorphism) and crystal structure, as well as occurrences of porosity and thorite inclusions in the Th-poor altered domains (Fig. 3), indicate that the alteration of bastnäsite is driven by a fluid-aided, coupled dissolution-reprecipitation process (Putnis 2002, 2009; Putnis and Putnis 2007; Hetherington and Harlov 2008). Fluid-aided coupled dissolution-reprecipitation is a well-established chemical reaction driven by a minimization in the Gibbs free energy (Putnis 2009). During this process, replacement of the original bastnäsite by altered bastnäsite is facilitated by a fluid boundary layer, supersaturated with respect to the altered bastnäsite between the altered and unaltered bastnäsite. The dissolved original bastnäesite can serve as a major source for the precipitation of secondary bastnäesite. Because of their textural epitaxial relationship, the original bastnäsite acts as a template from which the altered bastnäsite grows as the original bastnäsite is being replaced. The widespread porosity in the altered areas (Fig. 3) is due to a solubility discrepancy between the precipitated and primary bastnäsite phases (Putnis 2002, 2009). This porosity is essential to maintain the replacement to proceed as it provides a means for fluid infiltration.

The coupled dissolution-reprecipitation process is characterized by mass transport between the solid phase (bastnäsite) and hydrothermal fluids surrounding the bastnäsite via interconnected porosity in the altered areas of the bastnäsite (Putnis and Putnis 2007; Putnis 2009; Ruiz-Agudo et al. 2014). This explains the discrepancy in the U and Th contents between the unaltered and altered domains in the bastnäsite (Fig. 5d). U and Th mobilization during the dissolution-reprecipitation processes has also been documented in other geochronometers, such as monazite and xenotime (e.g., Hetherington and Harlov 2008; Hetherington et al. 2010; Harlov et al. 2011; Budzyń and Sláma 2019). The Pb contents in the unaltered and altered domains are not available in this study. However, inclusions of galena have been identified in the altered domains on both the micro- and nanoscales (Figs. 3 and 8d). These inclusions could not have formed from pre-existing radiogenic and/or non-radiogenic Pb through redis-
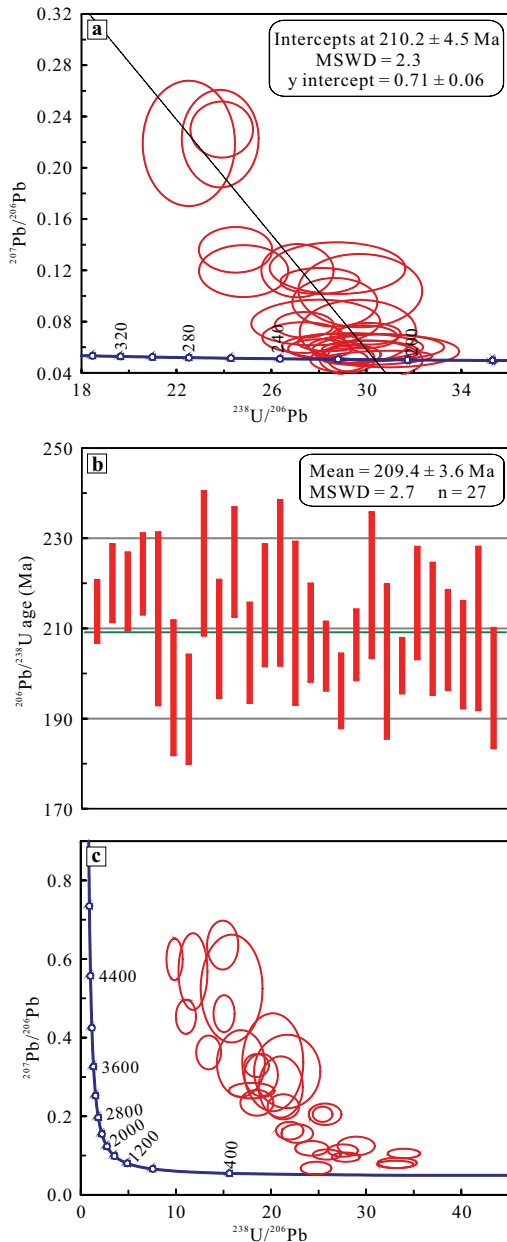
Figure 6. LA-ICP-MS U-Pb ages of both unaltered and altered domains in bastnäsite. (**a**) Tera-Wasserburg concordia diagram of uncorrected U-Pb data in the primary unaltered domains (uncertainty ellipses are 2σ). (**b**) Weighted average $^{206}Pb/^{238}U$ ages of the primary unaltered domains (^{207}Pb-based corrected; uncertainty bars are 2σ). (**c**) Tera-Wasserburg concordia diagram of uncorrected U-Pb data in the altered domains (uncertainty ellipses are 2σ).

Figure 7. Weighted average $^{208}Pb/^{232}Th$ age of the unaltered (**a**) and altered (**b**) domains in the bastnäsite (uncertainty bars are 2σ). Molybdenite Re-Os ages from the quartz-calcite-fluorite veins and quartz-pyrite veins are from Cao et al. (2014) and Li (2014).

tribution, as has been recorded in zircon (e.g., Kusiak et al. 2013; Whitehouse et al. 2014) and monazite (Seydoux-Guillaume et al. 2019). This is because the formation of Pb-rich inclusions during the dissolution-reprecipitation process requires a significant decrease of Pb in the altered domains. However, this is inconsistent with the fact that the altered domains generally have higher $^{206}Pb/^{238}U$ ratios than the unaltered domains (Online

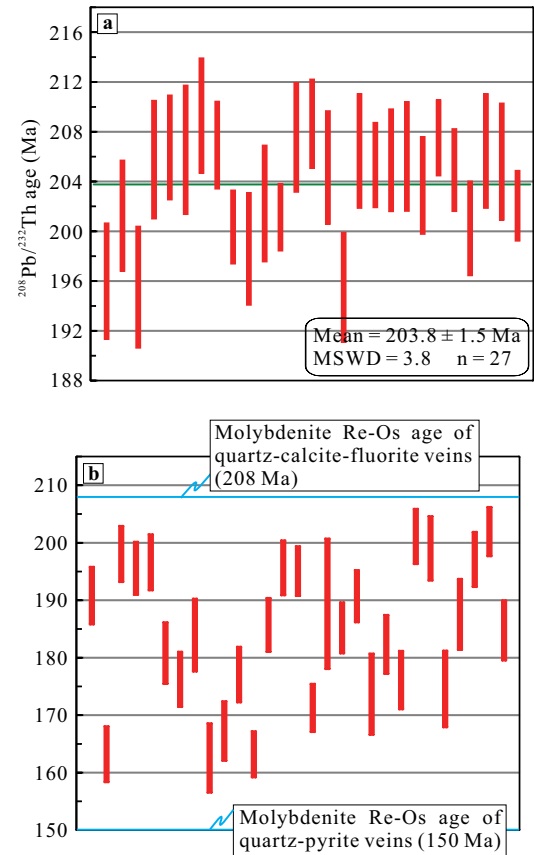Materials[1] Table OM3). In addition, the primary domains contain 5000 ppm of Th and 50 ppm of U (Online Materials[1] Table OM2), which would result in only 10 ppm of radiogenic Pb over a period from 208 to 150 Ma. Such a low Pb content would be unable to form the abundant galena inclusions in the altered domains (Fig. 3). Therefore, we propose that the Pb in these inclusions is non-radiogenic in origin (common Pb) and was incorporated into the altered domains from the late hydrothermal fluid during the coupled dissolution-reprecipitation process (Fig. 10). This interpretation is supported by the high Pb content in the fluids responsible for the alteration of the bastnäsite, as evidenced by the widespread occurrence of galena in the late quartz-pyrite veins (Fig. 2d).

Modification of $^{206}Pb/^{238}U$ and $^{207}Pb/^{206}Pb$ ages due to mobilization of U and Pb

Our results show that the altered domains have significantly higher $^{206}Pb/^{238}U$ and $^{207}Pb/^{206}Pb$ ratios than the unaltered domains (Fig. 6). These unexpected results are ascribed to the mobilization of U and Pb during the coupled dissolution-reprecipitation process. Here U is decreased (Fig. 5d), whereas common Pb is incorporated as shown by the galena inclusions in the altered areas of the bastnäsite. Incorporation of common Pb and loss

of U raise the ^{206}Pb/^{238}U ratio in the U-Pb system, resulting in unrealistically older ^{206}Pb/^{238}U ages. In addition, since common Pb has a relatively high ^{207}Pb/^{206}Pb ratio of 0.85 at 150 Ma (Stacey and Kramers 1975), its incorporation will significantly elevate the ^{207}Pb/^{206}Pb ages.

The highly variable ^{206}Pb/^{238}U and ^{207}Pb/^{206}Pb ratios on the Tera-Wasserburg plot (Fig. 6c) indicate a heterogeneity in the non-radiogenic Pb (common Pb) for the analyzed spots in the altered domains of the bastnäsite. Based on the U contents and ^{206}Pb/^{238}U ratios (Online Materials[1] Tables OM2 and OM3), the maximum amounts of non-radiogenic ^{206}Pb in the altered domains are estimated to be only 0.1 to 2.2 ppm (average at 0.6 ppm), assuming that the original radiogenic ^{206}Pb was completely removed during the replacement process. This demonstrates that due to the low contents of U and its daughter isotopes in bastnäsite, even minor incorporation of common Pb during the replacement will have a great influence on the U-Pb ages.

Partial resetting of ^{208}Pb/^{232}Th ages due to incomplete replacement

In contrast to the ^{206}Pb/^{238}U and ^{207}Pb/^{206}Pb ages, the ^{208}Pb/^{232}Th ages of the altered domains are all reasonably younger than those of the unaltered domains (Fig. 7), which tends to limit the effects of common Pb incorporation on the ^{208}Pb/^{232}Th ages. The key reason is that the bastnäsite has a dramatically high Th compared to U (Online Materials[1] Table OM2). For example, while some Th is lost during alteration, the altered domains consistently maintain high Th contents of about 3000 ppm (Fig. 5d; Online Materials[1] Table OM2). On the basis of this Th content, the amount of radiogenic ^{208}Pb produced by the decay of ^{232}Th over 150 Ma is estimated to be 23 ppm according to a decay constant of $\lambda_{Th232} = 4.9475e^{-11}$ year^{-1} (Steiger and Jäger 1977). On the other hand, based on the calculated non-radiogenic ^{206}Pb (i.e., average 0.6 ppm) and the ^{208}Pb/^{206}Pb ratio (2.07) for common Pb at 150 Ma (Stacey
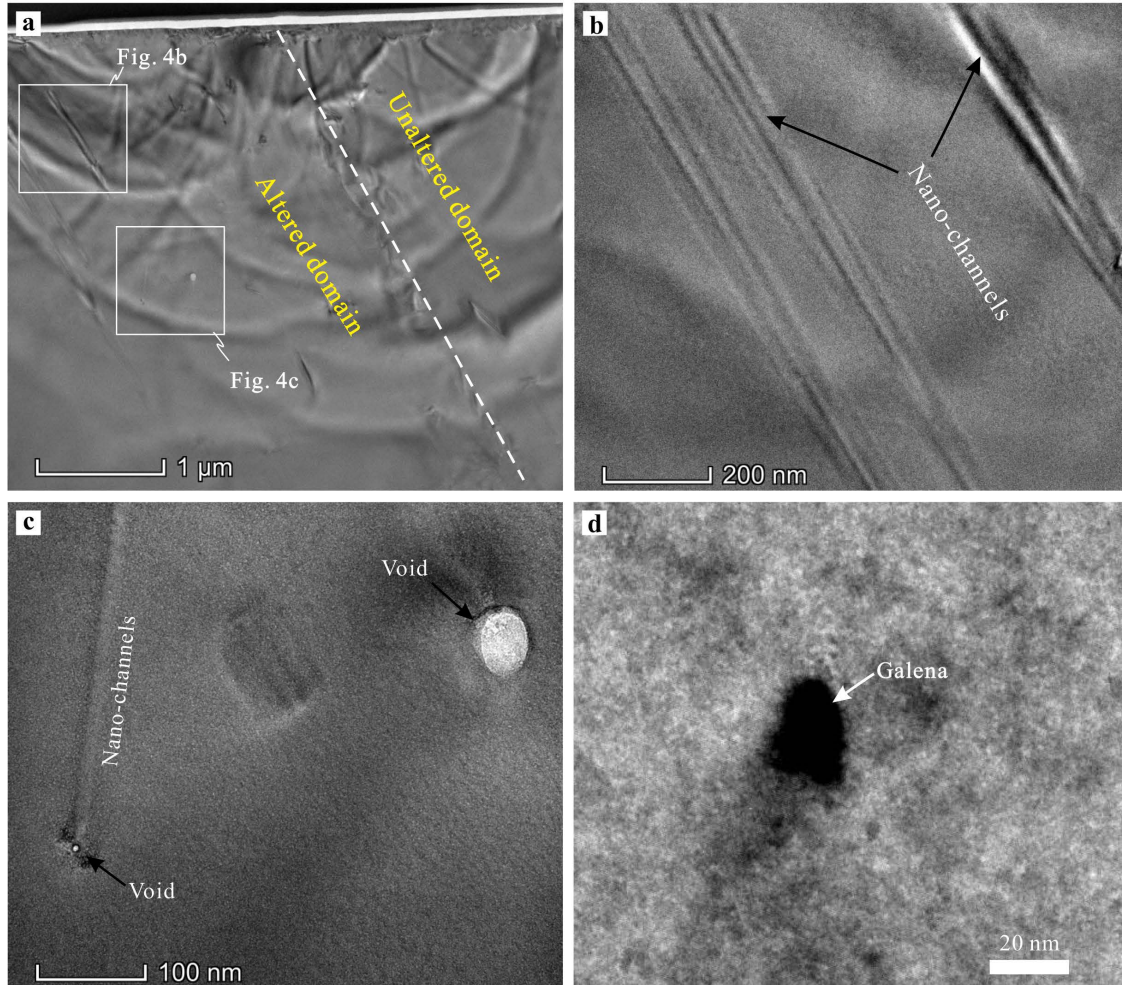

FIGURE 8. Transmission electron microscope (TEM) images of the altered bastnäsite. (**a**) TEM foil from Figure 3a. Also shown is the interface between the altered and unaltered bastnäsite. (**b**) Several parallel nano-channels in the altered domain. (**c**) Location of voids in the altered domain. (**d**) Nanoscale galena inclusions in the altered domain.
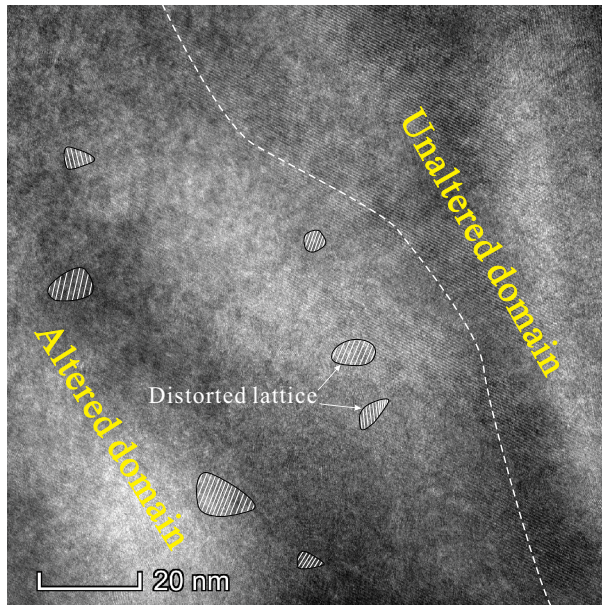
FIGURE 9. High-resolution TEM image of the interface between altered and unaltered domains. Note that the lattice fringes in the altered domain are frequently distorted with a random orientation.

and Kramers 1975), the amount of non-radiogenic ^{208}Pb in the analyzed spots of the altered domain is constrained to be only 1 ppm. These results indicate that the effect of non-radiogenic ^{208}Pb on the ^{208}Pb/^{232}Th ages is generally less than 5% (1:23). Therefore, it is concluded that incorporation of common Pb during the coupled dissolution-reprecipitation process has a limited effect on the ^{208}Pb/^{232}Th ages due to the high Th content in the bastnäsite.

As non-radiogenic ^{208}Pb is relatively negligible, the scattered ^{208}Pb/^{232}Th ages range from 208 to 150 Ma (Fig. 7b) in the altered domains could be ascribed to either protracted modification or incomplete replacement. Protracted modification can be excluded because the late quartz-pyrite veins have consistent molybdenite Re-Os ages of ~150 Ma (Li 2014), and other protracted magmatic-hydrothermal activities were not documented in the region. Instead, incomplete replacement during the dissolution-reprecipitation process has been documented in other geochronometers such as monazite (Harlov et al. 2011; Grand'Homme et al. 2016) and zircon (Harlov and Dunkley 2010). In the case of bastnäsite in the Huangshuian deposit, incomplete replacement is supported by the highly variable compositions of the altered domains that can occur even in a single grain (Fig. 5). In particular, the compositions of the altered domains partially overlap that of the unaltered domains (Fig. 5). This feature strongly indicates the existence of residual primary bastnäsite in the altered domains, leading to the partial retention of radiogenic ^{208}Pb (Fig. 10). It supports the conclusions that the Th-Pb system was partially reset during partial hydrothermal alteration of the bastnäsite, and that the obtained ^{208}Pb/^{232}Th ages in the altered domains represent a mixture of ages between the primary and newly precipitated bastnäsite.

GENERAL IMPLICATIONS

The results from this study reveal that the non-radiogenic Pb incorporated in Th-rich bastnäsite during the fluid-induced, coupled dissolution-reprecipitation process have significantly different impacts on its U-Pb and Th-Pb systems. The incorporation of non-radiogenic Pb seriously affected the U-Pb system due to the low U content in the bastnäsite. In addition to the incorporated non-radiogenic Pb, the bastnäsite was generally incompletely replaced during the alteration process allowing for residual radiogenic Pb to be left behind. These features make it unrealistic to correct the U-Pb ages in the altered domains (Fig. 6c). In such cases, the U-Pb dates do not record the timing of the alteration and thus should be treated with caution. Similar disturbances in the U-Pb system are also common in other chronometers, such as those documented in monazite from Ambato, Madagascar (Seydoux-Guillaume et al. 2012) and Velay Dome, France (Didier et al. 2013). Our results show that non-radiogenic Pb can occur as nanoscale inclusions of Pb-rich minerals such as galena, which thus cannot be identified by traditional microscopic and SEM methods. Therefore, a detailed investigation on the nature (especially the Pb content) of the fluids responsible for the re-
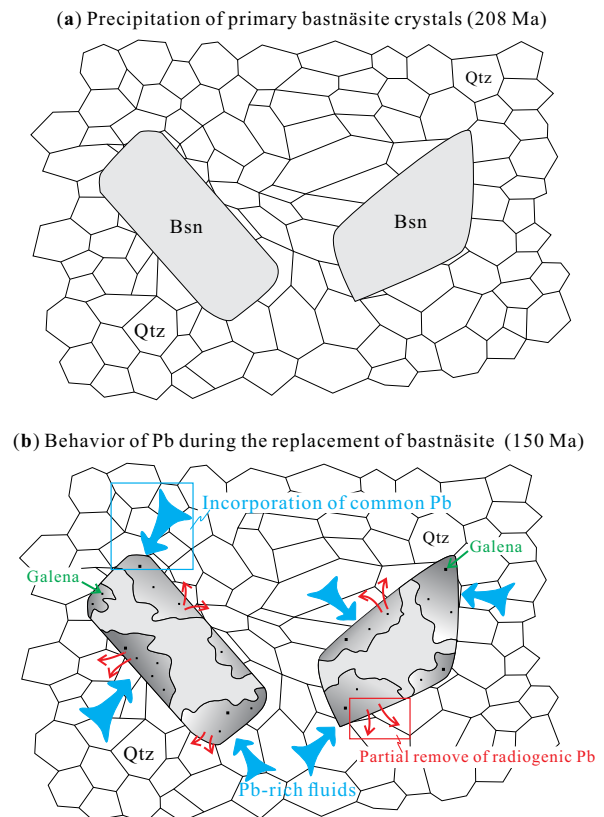
(a) Precipitation of primary bastnäsite crystals (208 Ma)

(b) Behavior of Pb during the replacement of bastnäsite (150 Ma)

FIGURE 10. Sketches illustrating the behavior of Pb during the alteration of bastnäsite in the Huanshuian deposit. (**a**) Precipitation of primary bastnäsite crystals during the intrusion of carbonatites at 208 Ma. (**b**) Hydrothermal overprint of bastnäsite at 150 Ma. Note that the non-radiogenic Pb (common Pb) is incorporated in the bastnäsite whereas the radiogenic Pb is partially removed due to incomplete replacement. See text for further details.

placement/alteration will help to facilitate the interpretation of discordant U-Pb ages for the altered domains.

In contrast to the U-Pb system, non-radiogenic Pb incorporation has limited effects on the Th-Pb system during alteration due to the remarkably high Th content in the bastnäsite. Instead, the Th-Pb system was variably affected by the partial removal of early radiogenic Pb due to incomplete replacement. Therefore, the scattered Th-Pb ages seen in the altered domains could be used to approximate the upper age limit for timing the secondary hydrothermal activity or approximate the lower age limit for timing the primary mineralization, depending on the degree of removal of the radiogenic Pb. The results from this study provide a potentially reasonable criterion by which to evaluate the significance of variable Th-Pb ages obtained from altered bastnäsite in specific REE deposits. For example, the bastnäsite and associated monazite from the Bayan Obo Fe-REE-Nb and Miaoya REE-Nb deposits, which suffered severe secondary hydrothermal modification, have scattered Th-Pb ages ranging from 1250 to 260 Ma (Smith et al. 2015; Song et al. 2018; Li et al. 2021) and from 430 to 206 Ma (Ying et al. 2017; Zhang et al. 2019), respectively. In summary, the U-Pb and Th-Pb ages in altered domains from bastnäsite may have different geological meanings and should be treated separately during the dating of secondary hydrothermal events in the REE deposits.

REFERENCES CITED

Budzyń, B. and Sláma, J. (2019) Partial resetting of U-Pb ages during experimental fluid-induced re-equilibration of xenotime. Lithos, 346–347, 105163, https://doi.org/10.1016/j.lithos.2019.105163.

Cao, J., Ye, H., Li, H., Li, Z., Zhang, X.K., He, W., and Li, C. (2014) Geological characteristics and molybdenite Re-Os isotopic dating of Huangshuian carbonatite vein-type Mo (Pb) deposit in Songxian County, Henan Province. Mineralium Deposita, 33, 53–69 (in Chinese with English abstract).

Deng, J., Gong, Q., Wang, C., Carranza, E.J.M., and Santosh, M. (2014) Sequence of Late Jurassic-Early Cretaceous magmatic-hydrothermal events in the Xiong'ershan region, Central China: An overview with new zircon U-Pb geochronology data on quartz porphyries. Journal of Asian Earth Sciences, 79, 161–172, https://doi.org/10.1016/j.jseaes.2013.09.018.

Didier, A., Bosse, V., Boulvais, P., Bouloton, J., Paquette, J.L., Montel, J.M., and Devidal, J.L. (2013) Disturbance versus preservation of U-Th-Pb ages in monazite during fluid–rock interaction: Textural, chemical and isotopic in situ study in microgranites (Velay Dome, France). Contributions to Mineralogy and Petrology, 165, 1051–1072, https://doi.org/10.1007/s00410-012-0847-0.

Dong, Y. and Santosh, M. (2016) Tectonic architecture and multiple orogeny of the Qinling Orogenic Belt, Central China. Gondwana Research, 29, 1–40, https://doi.org/10.1016/j.gr.2015.06.009.

Grand'Homme, A., Janots, E., Seydoux-Guillaume, A.M., Guillaume, D., Bosse, V., and Magnin, V. (2016) Partial resetting of the U-Th-Pb systems in experimentally altered monazite: Nanoscale evidence of incomplete replacement. Geology, 44, 431–434, https://doi.org/10.1130/G37770.1.

Harlov, D.E. and Dunkley, D., (2010) Experimental high-grade alteration of zircon using alkali- and Ca-bearing solutions: resetting the zircon geochronometer during metasomatism. V41D–2301 presented at 2010 Fall Meeting, AGU, San Francisco, California, 13–17 December.

Harlov, D.E., Wirth, R., and Hetherington, C.J. (2011) Fluid-mediated partial alteration in monazite: The role of coupled dissolution-reprecipitation in element redistribution and mass transfer. Contributions to Mineralogy and Petrology, 162, 329–348, https://doi.org/10.1007/s00410-010-0599-7.

He, Y., Zhao, G., Sun, M., and Xia, X. (2009) SHRIMP and LA-ICP-MS zircon geochronology of the Xiong'er volcanic rocks: Implications for the Paleo-Mesoproterozoic evolution of the southern margin of the North China Craton. Precambrian Research, 168, 213–222, https://doi.org/10.1016/j.precamres.2008.09.011.

Hetherington, C.J. and Harlov, D.E. (2008) Metasomatic thorite and uraninite inclusions in xenotime and monazite from granitic pegmatites, Hidra anorthosite massif, southwestern Norway: Mechanics and fluid chemistry. American Mineralogist, 93, 806–820, https://doi.org/10.2138/am.2008.2635.

Hetherington, C.J., Harlov, D.E., and Budzyń, B. (2010) Experimental metasomatism of monazite and xenotime: Mineral stability, REE mobility and fluid composition. Mineralogy and Petrology, 99, 165–184, https://doi.org/10.1007/s00710-010-0110-1.

Hu, Z., Zhang, W., Liu, Y., Gao, S., Li, M., Zong, K., Chen, H., and Hu, S. (2015) "Wave" signal-smoothing and mercury-removing device for laser ablation quadrupole and multiple collector ICPMS analysis: Application to lead isotope analysis. Analytical Chemistry, 87, 1152–1157, https://doi.org/10.1021/ac503749k.

Jordens, A., Cheng, Y.P., and Waters, K.E. (2013) A review of the beneficiation of rare earth element bearing minerals. Minerals Engineering, 41, 97–114, https://doi.org/10.1016/j.mineng.2012.10.017.

Kröner, A., Compston, W., Zhang, G.W., Gu, A., and Todt, W. (1988) Age and tectonic setting of Late Archean greenstone-gneiss terrain in Henan Province, China, as revealed by single-grain zircon dating. Geology, 16, 211–215, https://doi.org/10.1130/0091-7613(1988)016<0211:AATSOL>2.3.CO;2.

Kusiak, M.A., Whitehouse, M.J., Wilde, S.A., Nemchin, A.A., and Clark, C. (2013) Mobilization of radiogenic Pb in zircon revealed by ion imaging: Implications for early Earth geochronology. Geology, 41, 291–294, https://doi.org/10.1130/G33920.1.

Kynicky, J., Smith, M.P., and Xu, C. (2012) Diversity of rare earth deposits: The key example of China. Elements (Quebec), 8, 361–367, https://doi.org/10.2113/gselements.8.5.361.

Li, J.H. (2014) Re-Os isotopic dating of molybdenites from the Dashimengou molybdenum deposit in Songxian County, Henan Provinces, and its geological significance. Geology in China, 41, 1364–1374 (in Chinese with English abstract).

Li, N. and Pirajno, F. (2017) Early Mesozoic Mo mineralization in the Qinling Orogen: An overview. Ore Geology Reviews, 81, 431–450, https://doi.org/10.1016/j.oregeorev.2016.03.008.

Li, X.C., Yang, K.F., Spandler, C., Fan, H.R., Zhou, M.F., Hao, J.L., and Yang, Y.H. (2021) The effect of fluid-aided modification on the Sm-Nd and Th-Pb geochronology of monazite and bastnäsite: Implication for resolving complex isotopic age data in REE ore systems. Geochimica et Cosmochimica Acta, 300, 1–24, https://doi.org/10.1016/j.gca.2021.02.028.

Ling, X.X., Li, Q.L., Liu, Y., Yang, Y.H., Liu, Y., Tang, G.Q., and Li, X.H. (2016) In-situ SIMS Th–Pb dating of bastnaesite: Constraint on the mineralization time of the Himalayan Mianning-Dechang rare earth element deposits. Journal of Analytical Atomic Spectrometry, 31, 1680–1687, https://doi.org/10.1039/C6JA00093B.

Liu, Y.S., Hu, Z.C., Gao, S., Günther, D., Xu, J., Gao, C.G., and Chen, H.H. (2008) In situ analysis of major and trace elements of anhydrous minerals by LA-ICP-MS without applying an internal standard. Chemical Geology, 257, 34–43, https://doi.org/10.1016/j.chemgeo.2008.08.004.

Liu, Y., Gao, S., Hu, Z., Gao, C., Zong, K., and Wang, D. (2010) Continental and oceanic crust recycling-induced melt–peridotite interactions in the Trans-North China Orogen: U–Pb dating, Hf isotopes and trace elements in zircons from mantle xenoliths. Journal of Petrology, 51, 537–571, https://doi.org/10.1093/petrology/egp082.

Ludwig, K.R. (2003) Isoplot 3.00: A Geochronological Toolkit for Microsoft Excel. Berkeley Geochronology Center, http://books.google.com/books?id=OutNAQAAIAAJ.

Ma, R.L., Chen, T.W., Zhang, W., and Chen, Y.W. (2021) Hydrothermal upgrading as an important tool for the REE mineralization in the Miaoya carbonatite-syenite complex, Central China. American Mineralogist, 106, 1690–1703, https://doi.org/10.2138/am-2021-7779.

Mao, J.W., Xie, G.Q., Bierlein, F., Qü, W.J., Du, A.D., Ye, H.S., Pirajno, F., Li, H.M., Guo, B.J., Li, Y.F., and others. (2008) Tectonic implications from Re-Os dating of Mesozoic molybdenum deposits in the East Qinling–Dabie orogenic belt. Geochimica et Cosmochimica Acta, 72, 4607–4626, https://doi.org/10.1016/j.gca.2008.06.027.

Mao, J.W., Pirajno, F., Xiang, J.F., Gao, J.J., Ye, H.S., Li, Y.F., and Guo, B.J. (2011) Mesozoic molybdenum deposits in the east Qinling-Dabie orogenic belt: Characteristics and tectonic settings. Ore Geology Reviews, 43, 264–293, https://doi.org/10.1016/j.oregeorev.2011.07.009.

Peng, P., Zhai, M., Ernst, R.E., Guo, J., Liu, F., and Hu, B. (2008) A 1.78 Ga large igneous province in the North China craton: The Xiong'er volcanic province and the North China dyke swarm. Lithos, 101, 260–280, https://doi.org/10.1016/j.lithos.2007.07.006.

Putnis, A. (2002) Mineral replacement reactions: From macroscopic observations to microscopic mechanisms. Mineralogical Magazine, 66, 689–708, https://doi.org/10.1180/0026461026650056.

——— (2009) Mineral replacement reactions. Reviews in Mineralogy and Geochemistry, 70, 87–124.

Putnis, A. and Putnis, C.V. (2007) The mechanism of reequilibration of solids in the presence of a fluid phase. Journal of Solid State Chemistry, 180, 1783–1786, https://doi.org/10.1016/j.jssc.2007.03.023.

Ruiz-Agudo, E., Putnis, C.V., and Putnis, A. (2014) Coupled dissolution and precipitation at mineral-fluid interfaces. Chemical Geology, 383, 132–146, https://

doi.org/10.1016/j.chemgeo.2014.06.007.

Sal'nikova, E.B., Yakovleva, S.Z., Nikiforov, A.V., Kotov, A.B., Yarmolyuk, V.V., Anisimova, I.V., Sugorakova, A.M., and Plotkina, Y.V. (2010) Bastnaesite: A promising U-Pb geochronological tool. Doklady Earth Sciences, 430, 134–136, https://doi.org/10.1134/S1028334X10010290.

Schoene, B., (2014) U-Th-Pb Geochronology. In K. Turekian and H. Holland, Eds., Treatise on Geochemistry (2nd ed.), 4, 341–378.

Seydoux-Guillaume, A.M., Montel, J.M., Bingen, B., Bosse, V., de Parseval, P., Paquette, J.L., Janots, E., and Wirth, R. (2012) Low-temperature alteration of monazite: Fluid mediated coupled dissolution–precipitation, irradiation damage, and disturbance of the U-Pb and Th-Pb chronometers. Chemical Geology, 330–331, 140–158, https://doi.org/10.1016/j.chemgeo.2012.07.031.

Seydoux-Guillaume, A.M., Fougerouse, D., Laurent, A.T., Gardés, E., Reddy, S.M., and Saxey, D.W. (2019) Nanoscale resetting of the Th/Pb system in an isotopically-closed monazite grain: A combined atom probe and transmission electron microscopy study. Geoscience Frontiers, 10, 65–76, https://doi.org/10.1016/j.gsf.2018.09.004.

Smith, M.P., Campbell, L.S., and Kynicky, J. (2015) A review of the genesis of the world class Bayan Obo Fe-REE-Nb deposits, Inner Mongolia, China: Multistage processes and outstanding questions. Ore Geology Reviews, 64, 459–476, https://doi.org/10.1016/j.oregeorev.2014.03.007.

Song, W., Xu, C., Smith, M.P., Kynicky, J., Huang, K., Wei, C., Zhou, L., and Shu, Q. (2016) Origin of unusual HREE-Mo-rich carbonatites in the Qinling orogen, China. Scientific Reports, 6, 37377, https://doi.org/10.1038/srep37377.

Song, W., Xu, C., Smith, M.P., Chakhmouradian, A.R., Brenna, M., Kynicky, J., Chen, W., Yang, Y., Deng, W., and Tang, H. (2018) Genesis of the world's largest rare earth element deposit, Bayan Obo, China: Protracted mineralization evolution over ~ 1 b.y. Geology, 46, 323–326, https://doi.org/10.1130/G39801.1.

Stacey, J.S. and Kramers, J.D. (1975) Approximation of terrestrial lead isotope evolution by a two stage model. Earth and Planetary Science Letters, 26, 207–221, https://doi.org/10.1016/0012-821X(75)90088-6.

Steiger, R.H. and Jäger, E. (1977) Subcommission on geochronology: Convention on the use of decay constants in geo-and cosmochronology. Earth and Planetary Science Letters, 36, 359–362, https://doi.org/10.1016/0012-821X(77)90060-7.

Weng, Z., Jowitt, S.M., Mudd, G.M., and Haque, N. (2015) A detailed assessment of global rare earth element resources: Opportunities and challenges. Economic Geology and the Bulletin of the Society of Economic Geologists, 110, 1925–1952, https://doi.org/10.2113/econgeo.110.8.1925.

Whitehouse, M.J., Ravindra Kumar, G.R., and Rimša, A. (2014) Behaviour of radiogenic Pb in zircon during ultrahigh-temperature metamorphism: An ion imaging and ion tomography case study from the Kerala Khondalite Belt, southern India. Contributions to Mineralogy and Petrology, 168, 1042, https://doi.org/10.1007/s00410-014-1042-2.

Williams, M.L., Jercinovic, M.J., Harlov, D.E., Budzyń, B., and Hetherington, C.J. (2011) Resetting monazite ages during fluid-related alteration. Chemical Geology, 283, 218–225, https://doi.org/10.1016/j.chemgeo.2011.01.019.

Wirth, R. (2004) Focused Ion Beam (FIB): A novel technology for advanced application of micro- and nanoanalysis in geosciences and applied mineralogy. European Journal of Mineralogy, 16, 863–876, https://doi.org/10.1127/0935-1221/2004/0016-0863.

Wu, Y.B. and Zheng, Y.F. (2013) Tectonic evolution of a composite collision orogen: An overview on the Qinling–Tongbai–Hong'an–Dabie–Sulu orogenic belt in central China. Gondwana Research, 23, 1402–1428, https://doi.org/10.1016/j.gr.2012.09.007.

Yang, Y.H., Wu, F.Y., Li, Y., Yang, J.H., Xie, L.W., Liu, Y., Zhang, Y.B., and Huang, C. (2014) In-situ U-Pb dating of bastnaesite by LA-ICP-MS. Journal of Analytical Atomic Spectrometry, 29, 1017–1023, https://doi.org/10.1039/C4JA00001C.

Yang, Y.H., Wu, F.Y., Li, Q.L., Rojas-Agramonte, Y., Yang, J.H., Li, Y., Ma, Q., Xie, L.W., Huang, C., Fan, H.R., and others. (2019) In situ U-Th-Pb dating and Sr-Nd isotope analysis of bastnäsite by LA-(MC)-ICP-MS. Geostandards and Geoanalytical Research, 43, 543–565, https://doi.org/10.1111/ggr.12297.

Ying, Y.C., Chen, W., Lu, J., Jiang, S.Y., and Yang, Y.H. (2017) In situ U-Th-Pb ages of the Miaoya carbonatite complex in the South Qinling orogenic belt, central China. Lithos, 290-291, 159–171, https://doi.org/10.1016/j.lithos.2017.08.003.

Ying, Y.C., Chen, W., Simonetti, A., Jiang, S.Y., and Zhao, K.D. (2020) Significance of hydrothermal reworking for REE mineralization associated with carbonatite: Constraints from in situ trace element and C-Sr isotope study of calcite and apatite from the Miaoya carbonatite complex (China). Geochimica et Cosmochimica Acta, 280, 340–359, https://doi.org/10.1016/j.gca.2020.04.028.

Zhang, G.W., Zhang, B.R., Yuan, X.C., and Xiao, Q.H. (2001) Qinling Orogenic Belt and Continental Dynamics, 1–806. Science Press (in Chinese).

Zhang, W., Chen, W.T., Gao, J.F., Chen, H.K., and Li, J.H. (2019) Two episodes of REE mineralization in the Qinling Orogenic Belt, Central China: In-situ U-Th-Pb dating of bastnäsite and monazite. Mineralium Deposita, 54, 1265–1280, https://doi.org/10.1007/s00126-019-00875-7.

Zhang, W., Chen, H.K., Li, J.H., Chen, W.T., Zhang, X.C., and Tang, Y.W. (2021) Composition of ore-forming fluids in the Huangshuian carbonatite-related Mo-(REE) deposit: Insights from LA-ICP-MS analyses of fluid inclusions. Ore Geology Reviews, 136, 104284, https://doi.org/10.1016/j.oregeorev.2021.104284.

Zhao, T.P., Zhou, M.F., Zhai, M., and Xia, B. (2002) Paleoproterozoic rift-related volcanism of the Xiong'er Group, North China Craton: Implications for the breakup of Columbia. International Geology Review, 44, 336–351, https://doi.org/10.2747/0020-6814.44.4.336.

Zhao, G., He, Y., and Sun, M. (2009) The Xiong'er volcanic belt at the southern margin of the North China Craton: Petrographic and geochemical evidence for its outboard position in the Paleo-Mesoproterozoic Columbia Supercontinent. Gondwana Research, 16, 170–181, https://doi.org/10.1016/j.gr.2009.02.004.

Zong, K.Q., Klemd, R., Yuan, Y., He, Z.Y., Guo, J.L., Shi, X.L., Liu, Y.S., Hu, Z.C., and Zhang, Z.M. (2017) The assembly of Rodinia: The correlation of early Neoproterozoic (ca. 900 Ma) high-grade metamorphism and continental arc formation in the southern Beishan Orogen, southern Central Asian Orogenic Belt (CAOB). Precambrian Research, 290, 32–48, https://doi.org/10.1016/j.precamres.2016.12.010.

Endnote:

[1]Deposit item AM-23-38318, Online Materials. Deposit items are free to all readers and found on the MSA website, via the specific issue's Table of Contents (go to http://www.minsocam.org/MSA/AmMin/TOC/2023/Mar2023_data/Mar2023_data.html).